Phased Array Focusing for Acoustic Wireless Power Transfer

Victor Farm-Guoo Tseng, Sarah S. Bedair, *Associate Member, IEEE*, and Nathan Lazarus

Abstract—**Wireless power transfer (WPT) through acoustic waves can achieve higher efficiencies than inductive coupling when the distance is above several times the transducer size. This paper demonstrates the use of ultrasonic phased arrays to focus power to receivers at arbitrary locations to increase the power transfer efficiency. Using a phased array consisting of 37 elements at a distance nearly five times the receiver transducer diameter, a factor of 2.6 increase in efficiency was achieved when compared to a case equivalent to a single large transducer with the same peak efficiency distance. The array has a total diameter of 7 cm, and transmits through air at 40 kHz to a 1.1 cm diameter receiver, achieving a peak overall efficiency of 4% at a distance of 5 cm. By adjusting the focal distance, the efficiency can also be maintained relatively constant at distances up to 9 cm. Numerical models were developed and shown to closely match the experimental energy transfer behavior; modeling results indicate that the efficiency can be further doubled by increasing the number of elements. For comparison, an inductive WPT system was also built with the diameters of the transmitting and receiving coils equivalent to the dimensions of the transmitting ultrasonic phased array and receiver transducer, and the acoustic WPT system achieved higher efficiencies than the inductive WPT system when the transmit-to-receive distance is above 5 cm. Additionally, beam angle steering was demonstrated by using a simplified 7 element 1D array, achieving power transfer less dependent on receiver placement.**

Index Terms—**Ultrasonic transducers, phased arrays, wireless power transfer (WPT), contactless energy transfer (CET), acoustic focusing, beam steering.**

I. INTRODUCTION

THE market for wireless power transmission (WPT) has grown rapidly in the recent years, largely due to the heightened consumer awareness of the technology [1]. By eliminating cabling or batteries, WPT brings the benefit of reducing system size and weight, allowing for power delivery to inaccessible locations, and enabling dynamic (in motion) charging [2]. Integrating wireless capabilities is therefore highly desirable in applications such as consumer electronics [3], biomedical implants [4]–[9], electric vehicle charging [10], [11], and powering devices in remote or harsh environments [12], [13].

Methods currently used for WPT can be categorized into two groups: radiative (such as microwave and laser transmission) and non-radiative (such as inductive and capacitive coupling). Radiative methods provide the capability of power beaming to remote targets but usually have lower overall efficiency (with reasonable size at far-field distance) [13]–[20], while non-radiative methods typically provide higher power transfer efficiency (>70%) but are limited to shorter ranges [21]–[24]. Due to the longer wavelengths used for microwave transmission, the size of the transmitter/receiver are usually prohibitively large [13]–[17], while high-power solid-state microwave generation is still rather difficult [13] due to the power handling and parasitics of the components. Laser transmission offers the best focusing ability among all methods, but is limited by the typically lower conversion efficiencies [18], [19], and is very sensitive to atmospheric conditions [20]. Amongst the non-radiative methods, capacitive coupling offers the benefit of freedom of placement, but can only operate within very small distances (<1 mm) and requires very high voltages [21]. Currently, inductive coupling is still the *de facto* standard for WPT, attracting considerable research attention [21]–[24]. Magnetic resonant coupling [24] can also be incorporated to extend the charging distance. However, larger coils with extremely high quality factors are needed to achieve longer distances, and the charging distance is still limited to a few coil diameters, after which the efficiency decreases rapidly [3], [7], [24], [28].

Rather than using electromagnetic waves, achieving WPT through acoustic/ultrasonic waves has been recently proposed [25]–[32]. Due to the much shorter wavelengths at the same frequency, acoustic transmitters can achieve higher beam directivity than electromagnetic transmitters of the same size. When compared to inductive WPT, acoustic WPT can achieve higher efficiencies when the distance is above several times the transducer/coil size [7], [28]. Due to the much lower frequencies used compared to microwave or inductive WPT, switching losses become much less significant, and the design of the associated electronics can be kept relatively simple as well [27]. Furthermore, by using different types of transducers, acoustic WPT through various mediums, such as air, human tissue [29], and metal [30] (which shields off high frequency electromagnetic fields), can also be achieved. The feasibility of through-air acoustic WPT was demonstrated by Roes [26],

showing that for a chosen distance and transducer size there is an optimum frequency to maximize efficiency. However, in the near-field region, there are significant spatial fluctuations in acoustic intensity due to wave interference, leading to locations where power cannot be transferred, while the efficiency drops rapidly when the receiver is not centered on the acoustic beam.

In this work, we demonstrate for the first time the usage of an ultrasonic phased array to enhance the performance of through-air acoustic WPT. By using a phased array transmitter instead of a transducer with the same diameter as the array, acoustic focusing can be used to increase the efficiency within the near-field region (utilized in [33], [34] for imaging applications). This enables focal distance tuning, which helps maintain the efficiency relatively constant over a modest distance range. The improved acoustic power transfer through focusing was studied via finite element modeling, and the results were experimentally verified. An inductive WPT system with coils of the same size as the ultrasonic phased array and receiver was also built for comparison, which showcases the advantage of acoustic WPT at larger distances. We also demonstrate for the first time the usage of acoustic beam angle steering for off-axis power beaming (functional in both near-field and far-field regions), and the results were compared to numerical simulations. Note that this paper focuses on the proof-of-concept demonstration, while the optimization, adaptive feedback [8], and control circuitry [35], [36] that are needed to realize the full system potential are not investigated.
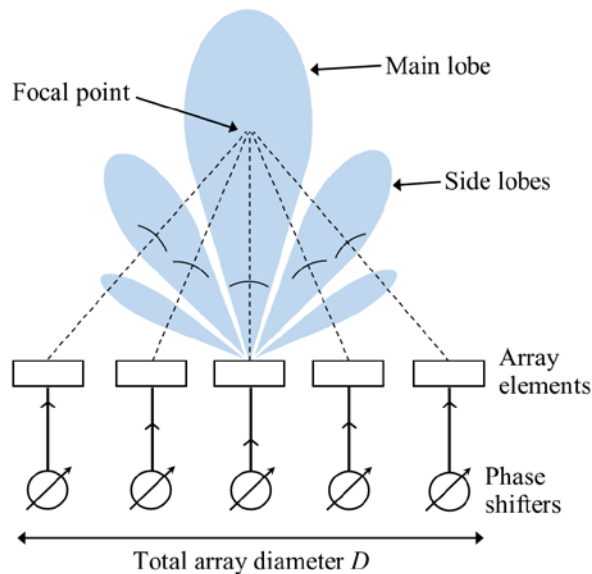

Fig. 1. 2D schematic of the phased array transmitter and radiation pattern.

II. Modeling of Acoustic Focusing

The overall efficiency is the product of the respective transducer efficiencies (the acoustic-electrical real power conversion efficiencies at the transmitter and receiver) and the acoustic transfer fraction (ATF). ATF is defined as the fraction of the acoustic power emitted from the transmitter that arrives at the receiver (i.e. the integral of acoustic intensity at the receiver area divided by the integral of acoustic intensity at the total transmitter area) without accounting for wave reflections

at the receiver. The transducer efficiencies are largely determined by the device design, and the transducer modeling and measurements will be discussed later in section IV-A. Note that the current transducer model does not account for wave reflections [27], however, the measured reflections in our current experimental construction are rather small (Fig. 12(a)), therefore the calculated efficiencies can serve as a reasonable approximation. In the current section, a study on the theoretically achievable ATF is first presented, which is influenced by the design of the phased array for acoustic focusing and the acoustic attenuation through air.

A 2D schematic of the phased array design is shown in Fig. 1. The array has a total size/diameter of D, and is discretized into numerous array elements, with each element connected to a phase shifter. By adjusting the phase delay between driving signals to compensate for path length differences [33], [34], the acoustic waves can be focused, resulting in an acoustic radiation pattern as shown. Most of the acoustic power is contained within the main lobe, however, if the inter-element spacing becomes too large, side lobes with substantially higher power will be formed, which are called grating lobes (discussed with more detail in section II-A).
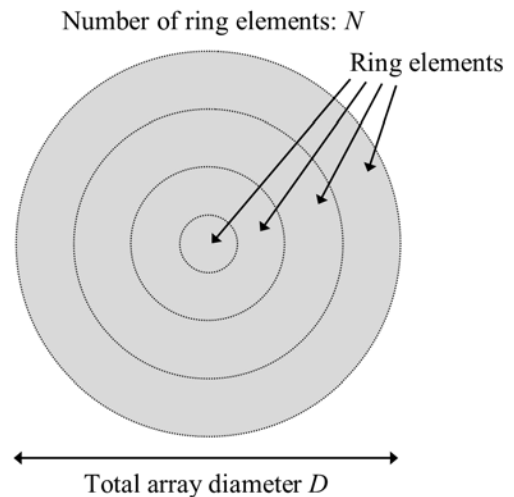

Fig. 2. Planar schematic view of the annular phased array discretized into ring elements used for simulations in section II.

The main parameters available to a designer are the number of elements and the total array diameter. Therefore, two separate studies were done via finite element simulations, one on varying the number of elements within an array of fixed total diameter (i.e. varying array discretization), and one on varying the total diameter of the array (i.e. varying total aperture). Since the elements of the physically constructed array are arranged in a hexagonal shaped layout (as presented in section III, shown in Fig. 8), for the simulations presented in this section, annular arrays discretized into constant width concentric ring elements were simulated in 2D axial symmetric mode to approximate the physically constructed array (planar schematic shown in Fig. 2). N is defined as the number of ring elements. All simulations were done at 40 kHz corresponding to the experimental conditions, with a 1.31 dB/m atmospheric attenuation incorporated [37]. To calculate the ATF, the

receiver diameter was kept constant as 1.1 cm to match the effective transducer area of the commercial device used as the receiver for measurements, and the receiver area was placed on the central axis of the transmitter array. The key simulation parameters used in this section are listed in Table I. No gap between adjacent ring elements was considered in the simulations of this section in order to investigate the maximum achievable ATF (the gap between elements is considered in the simulations of the physically constructed array presented in section III-A).

TABLE I
KEY SIMULATION PARAMETERS FOR SECTION II

Symbol	Definition	Value
D	Total array diameter	5-9 cm
N	Number of ring elements	3-11
z	Transmitter to receiver distance	2-14 cm
D_R	Receiver diameter	0.5-2 cm
f	Transmit/receive frequency	40 kHz
α	Atmospheric attenuation	1.31 dB/m
F	Set focal distance (adjustable)	>3 cm

A. Array Discretization

For this study, the total diameter D of the transmitting phased array was fixed to 7 cm to match the physically constructed array, while the number of ring elements N was varied. Note that the choice of 7 cm as the total array diameter and 1.1 cm as the receiver diameter was based on the availability of various commercial transducers, and these dimensions are only meant to serve as a proof-of-concept demonstration rather than an optimized design. The set focal distance F was adjusted by tuning the phase of each element based on path length difference calculations. A constant 1 Pa sound pressure magnitude was applied to each element, resulting in a constant input power. With F set as 6 cm, the simulated sound pressure level (SPL) and acoustic intensity radiation patterns from arrays with $N=4$ and $N=10$ are shown in Fig. 3 (intensity plotted with the same color scale to show the improved focusing of the $N=10$ case; receiver locations also shown for clarity). The intensity pattern from a large circular transducer with 7 cm diameter (the same size as the array) is also shown in Fig. 4, referred to as the case with no focusing (plotted with a smaller color scale for clarity; replotted with the same color scale as Fig. 3(b) and (d) in supplementary data Fig. S-1).

For the $N=4$ case, the acoustic transfer fraction (ATF) versus receiver distance z for various F set values is plotted in Fig. 5(a). The dotted line envelope represents the maximum ATF that can be achieved through adjusting F (hereby referred to as the achievable ATF). The 3dB roll-off is defined as the distance beyond the peak efficiency point at which the achievable ATF drops to 70.7% of the ATF at the peak efficiency. The peak ATF is 29% at around $z=6$ cm (5.6 times the receiver diameter) with F set as 6 cm. The increase in ATF through focusing can clearly be seen when compared to the case with no focusing (a single large transducer with 7 cm
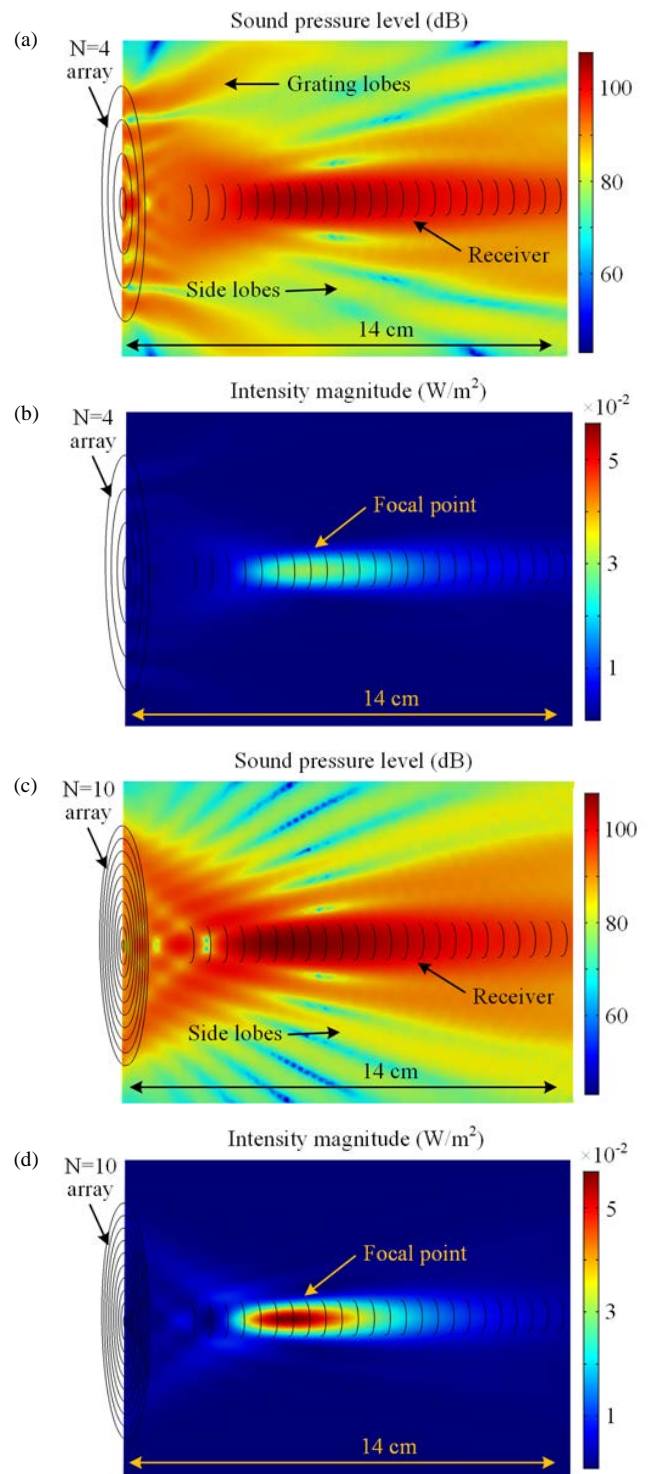

Fig. 3. Simulated radiation patterns from arrays with different discretization ($D=7$ cm, $F=6$ cm): (a) SPL from $N=4$ array, (b) intensity from $N=4$ array, (c) SPL from $N=10$ array, (d) intensity from $N=10$ array.

diameter). For a more valid comparison, the simulation results from the $D=7$ cm $N=4$ array with F set as 6 cm is compared to the simulation results from a single large transducer with 4.5 cm diameter (which has a peak efficiency at 6 cm), as plotted in Fig. 5(b). Compared at peak efficiency, the case with F set as 6 cm provides a near 2 times increase in ATF compared to the case with a 4.5 cm diameter single transducer. Such
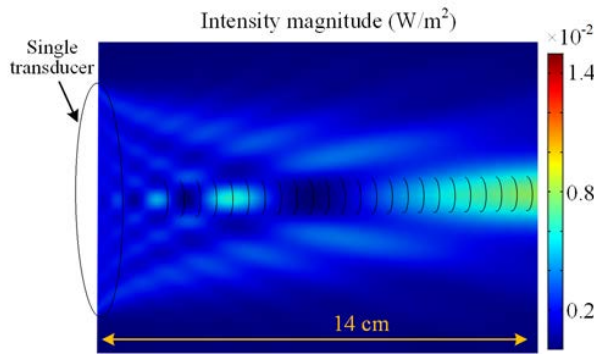
Fig. 4. Simulated intensity radiation pattern from a single large transducer with 7 cm diameter (plotted with a smaller color scale for clarity).

increase in ATF by acoustic focusing can only be achieved roughly within the near-field distance Z_{NF} (the location where the longest natural focal distance of the array occurs), which is 14 cm in this case. Z_{NF} can be approximated by using [34]

$$Z_{NF} \cong \frac{D^2 - \lambda^2}{4\lambda} \qquad (1)$$

with λ as the acoustic wavelength. The achievable ATF gradually decreases when $z>6$ cm, and the 3dB roll-off distance is at around $z=12$ cm. ATF also decreases at closer distances ($z<6$ cm) due to the limited radiation angle from each element, but the decrease in ATF can be reduced by using a larger N, or by activating the elements only within the inner portion of the array (with a cost of reducing the overall amount of power that is transferred). Note that by adjusting F, power can be transferred to any point within Z_{NF} without experiencing the spatial fluctuations in power as seen in the case with no focusing (Fig. 4, Fig. 5(a)).

As the number of ring elements N increases, the peak ATF consistently occurs within $z=5$ to 6 cm. As shown in Fig. 5(c), the peak ATF gradually increases with N until $N \geq 9$, after which it saturates at the maximum achievable ATF (~55%). This increase in ATF is due to the more effective contribution to the focal point from the smaller array elements at the outer portion of the array due to the wider radiation angles. The number of ring elements required to attain the maximum achievable ATF ($N \geq 9$) also coincides with the number of ring elements required to minimize grating lobes within the forward hemisphere ($\pm 90°$) of the array. Grating lobes are the result of spatial aliasing between the waves emitted from the array elements when the spacing between elements is too large [38]. Under continuous wave conditions, the maximum allowable inter-element spacing d_{max} without introducing grating lobes within the forward hemisphere ($\pm 90°$) of the array can be approximated by using

$$d_{max} = \lambda \frac{(N-1)}{2(N-1)+1} \qquad (2)$$

which is a modified equation from [34] with N as the number of ring elements (refer to Fig. 2). The inter-element spacing should be no larger than $\lambda/2$ (~0.43 cm) to attain the maximum achievable ATF. This can be seen by comparing the simulated sound pressure level patterns shown in Fig. 3(a) to Fig. 3(c), as

grating lobes with sound pressure levels comparable to the main lobe are visible in the $N=4$ case, but not visible in the $N=10$ case (only side lobes remaining). Comparing the intensity patterns in Fig. 3(b) and 3(d), the $F=10$ case shows higher peak intensity. In sum, it is desirable to have a larger number of elements within practical constraints.
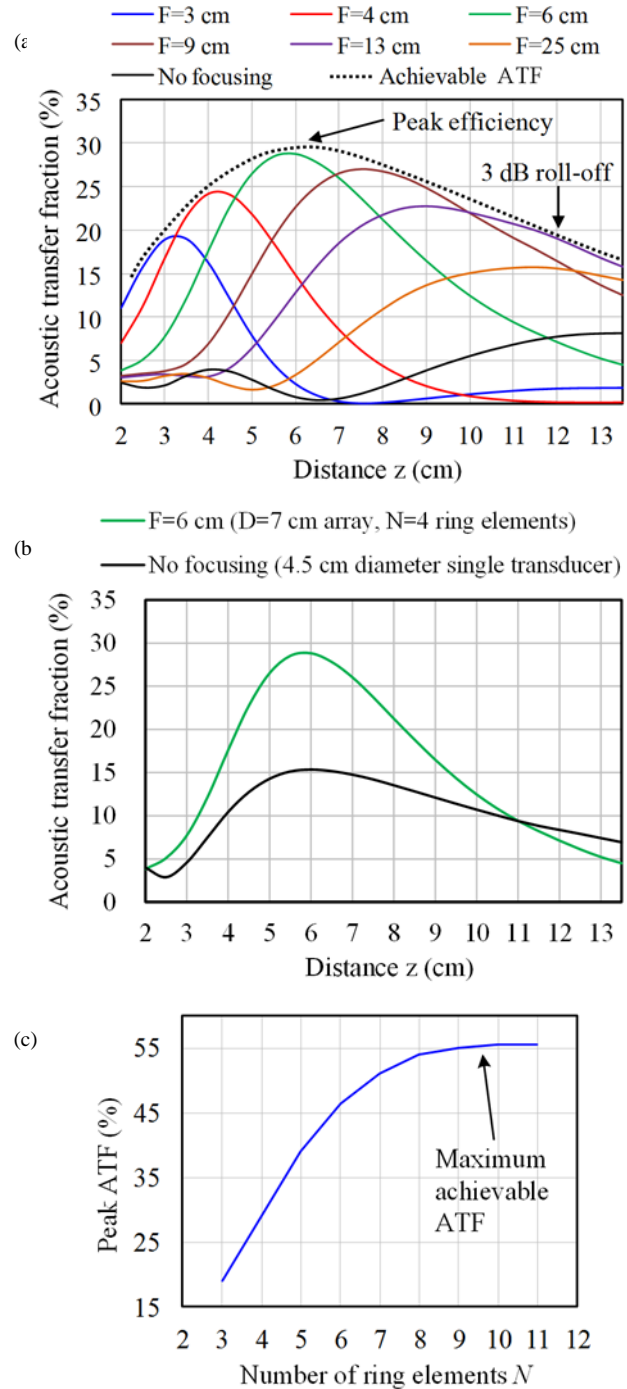

Fig. 5. Simulation results ($D=7$ cm, $R_d=1.1$ cm): (a) ATF versus distance z with various F set values ($N=4$), (b) ATF versus distance z for the $F=5$ cm, $N=4$ case compared to a 4.5 cm diameter single transducer (c) peak ATF versus N (peak ATF all occurring around $z=6$ cm with F set as 6 cm).

B. Array Size

The purpose of the second study was to investigate the effect of the total array diameter D on the ATF performance, therefore

the number of ring elements N was chosen to be large enough such that no grating lobes occur at the largest value of D, eliminating the influence of array discretization on the results. With N set as 11 and the receiver kept as the same size, the total diameter D of the array was then varied from 5 cm to 9 cm. For each case, the maximum achievable ATF stayed the same at around 55%, while the distance at which the peak efficiency and the 3 dB roll-off occurs steadily increases, as shown in Fig. 6. This is simply because a larger array has a larger near-field distance, and therefore a larger focal distance tuning range.

Note that the receiver diameter also has an effect on the peak ATF due to the larger diameter of the resolved focal point (as seen in Fig. 3(d)). With a constant D=7 cm, N=11, z=5 cm, and F set as 5 cm, simulations show that the peak ATF increases and saturates at 65% when the receiver diameter is enlarged to 1.5 cm (Fig. 7), therefore having a larger receiver size to cover the entire focal point is also desirable.
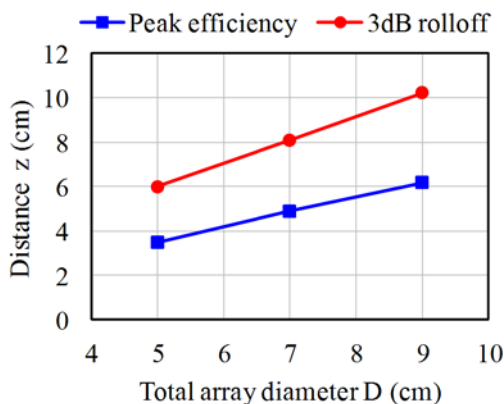

Fig. 6. Simulated distance at which the peak efficiency and 3dB roll-off occurs versus total array diameter D (R_d=1.1 cm).
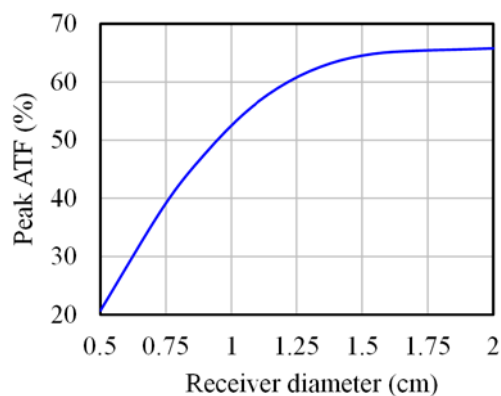

Fig. 7. Simulated maximum achievable ATF versus receiver diameter (D=7 cm, N=11, z=5 cm, F=5 cm).

III. DESIGN AND EXPERIMENTAL SETUP

A. Modeling and design of the 37 element array

The physically constructed phased array used for the measurements is shown in Fig. 8. The array is composed of 37 transducer elements tightly packed in a hexagonal array layout [36]. The inter-element spacing of 1 cm was limited by the physical dimensions of the transducers. In order to closely

match to the radiation beam angle of the commercial transducers used [39], the effective radiation area of each transducer in the best-fit model was approximately 0.84 cm, and this effective radiation area was used in the remaining simulations. The receiver diameter was kept as 1.1 cm to match the effective transducer area of the commercial device used for measurements. The simulations in this case were done in 3D FEM mode to accurately model the acoustic intensity pattern.
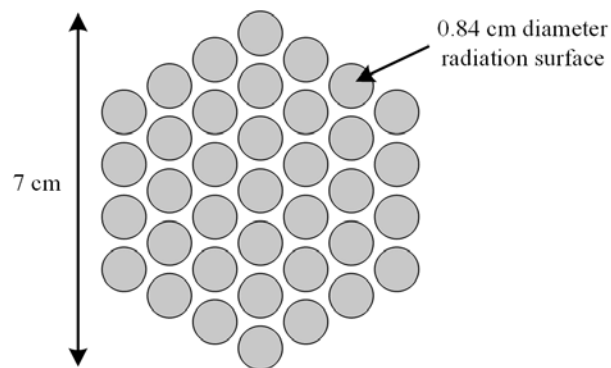

Fig. 8. Schematic of the 37 element phased array transmitter used for simulations and measurements.

With constant input power to all 37 transducers and the same phase delay calculations based on path length differences described in section II, the simulated radiation patterns from the 37 element array were very similar to Fig. 3(a) and (b) since the 37 element array can be essentially viewed as a four ring array. The simulated ATF versus distance for various F set values was also very similar to Fig. 5(a), showing a peak ATF of around 28%, and a focal distance tuning range within 14 cm. However, the distance at which the peak efficiency and 3 dB roll-off occurs are reduced to around z=5 cm and z=9 cm, respectively, which is primarily due to the wider radiation angle of each element caused by the slightly smaller element size. To further increase the ATF, it is desirable to increase the number of elements while maintaining a high array fill factor. The array fill factor may suffer if the gap between array transducers does not scale down with the transducer size itself. Therefore, one option would be to use standard microfabrication processes to produce an array with smaller sized tightly packed hexagonal shaped transducers [40]. As mentioned in section II-A, an ATF of 55% is expected to be achievable within the current dimensions.

B. Experimental Setup

The experimental setup for measuring the 37 element array is shown in Fig. 9. Murata MA40S4S transducers were used to assemble the 37 element transmitter array. The array transducers were carefully chosen to have the same polarity and closely matched series resonant frequencies f_{s_TX} (near 40.25 kHz). The MA40S4S has a 6 dB transmitting bandwidth of around 3 kHz. From the variety of transducers that were readily available, a Kobitone 255-400SR16-ROX transducer was chosen as the receiver due to its parallel resonant frequency f_{P_RX} of 40.40 kHz being close to the series resonant frequency f_{s_TX} of the array transducers (mismatch less than 150 Hz or

0.4%) since having a matched set of transducers to first order results in a higher, easier to measure output power [28], [36]. The 255-400SR16-ROX has a 6 dB receiving bandwidth of around 2.5 kHz. With the 37 element array fixed on a table, the receiver was positioned above the array with a precision linear stage used to adjust the location. The surrounding surfaces in proximity were covered with sound absorbing material made of fiberglass to avoid undesired reflections. A Wavetek-Datron multi-channel Model 195 waveform generator was used to generate multiple synchronized sinusoidal signals, then the signals were fed into opamp phase shifters to drive the 37 element phased array and provide phase fine tuning capability. The input power was determined by using 200 Ω series resistors to measure the input voltage V_{in} and current I_{in} waveforms to the array transducers, then multiplying V_{in} and I_{in} with regard to the phase difference to obtain the average real input power. Input power (voltage) as high as 10 mW (9 Vpp) was applied to each array transducer in order to reduce measurement errors. A potentiometer connected in parallel to the receiver was used as a tunable load resistor to measure the output power. No tuning inductors were used.
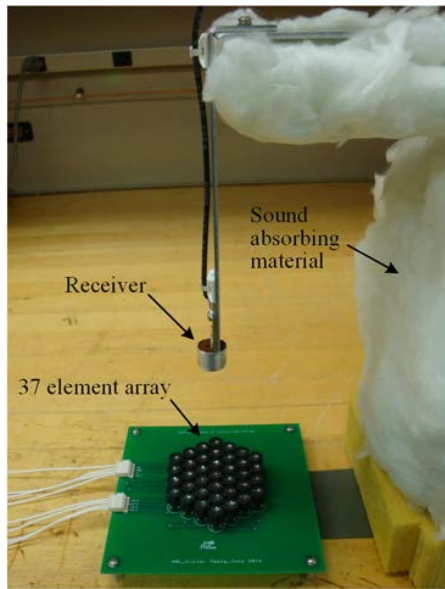

Fig. 9. Experimental setup for the focal distance tuning measurements using the 37 element array and the small receiver mounted on a precision linear stage.

IV. MEASUREMENT RESULTS

A. Transducer Efficiency

For realistic measurements, the acoustic impedance mismatch between the transducers and air as well as the electrical impedance mismatch between the receiver and the load will introduce additional power losses. To characterize the transducer efficiencies for the transmitter and receiver (considering only the real input/output power), all transducers were modeled by using the Butterworth-van Dyke equivalent circuit [28], and the circuit parameters were fitted by measuring the impedance of the transducers in air versus in vacuum [28] (impedance measurements in air shown in Fig. 10), thereby extracting the equivalent mechanical load resistance of air

exerted on the transducers R_a, and the equivalent mechanical load resistance from the transducer membrane itself R_m. From our measurements, the MA40S4S transmitter transducers has a R_a of 130 Ω and R_m of 77 Ω, and the 255-400SR16-ROX receiver transducer has a R_a of 1650 Ω and R_m of 100 Ω. With losses associated the transducer electrical capacitance being relatively small, the transducer efficiency for the transmitter transducers can be determined though [28]

$$\eta_{TX} = \frac{R_a}{R_a + R_m} . \qquad (3)$$

For a practical construction, an inductor in the driving electronics can be used to ring out the transmitter electrical capacitance to recover the energy stored on the input capacitive transducers. On the other hand, with no inductor incorporated in the receiver, the transducer efficiency for the receiver can be determined through [28]

$$\eta_{RX} = \frac{R_L}{R_L + R_m + \dfrac{R_m R_L^2}{X_e^2}} \qquad (4)$$

with R_L being the output load resistance and X_e being the reactance of the transducer electrical capacitance. At the optimal transmission frequency of 39.98 kHz, the average transducer efficiency for the 37 element array transmitter is around 63%, and the transducer efficiency for the receiver is around 33% (with an optimal load resistance of 1.7 kΩ). Although the receiver has a lower transducer efficiency, as mentioned above in section III-B, this particular transducer was chosen as the receiver from the readily available devices due to its f_{p_RX} being close to the f_{s_TX} of the array transducers in an attempt to minimize the effect of frequency mismatch and increasing the received output power [28], [36]. The lower receiver efficiency was mainly attributed to its larger impedance mismatch as well as multiple interfering harmonics close to its primary resonance (as shown in Fig. 10). Improved receiver designs should be able to bring the receiver efficiency closer to the transmitter efficiency. It should be noted that the Butterworth-van Dyke model was chosen due to its simplicity, and it takes into account all of the losses within the transducer, but it does not account for frequency dependent wave
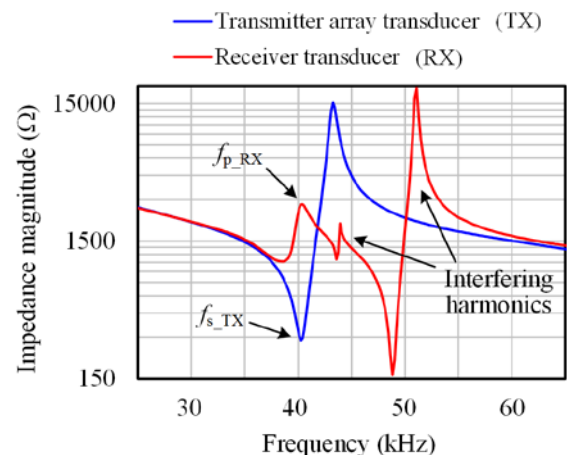

Fig. 10. Measured impedance magnitude versus frequency in air for the transmitter array transducers and the receiver transducer.

reflections (which requires more complicated modeling [7], [8]). However, the measured reflections in our current setup are rather small (Fig. 12(a)), therefore the calculated efficiencies can serve as a reasonable approximation to study the trend.

B. Focal Distance Tuning

The measured overall efficiency and corresponding acoustic transfer fraction (calculated with the measured transducer efficiencies presented above) versus receiver distance z for various F set values is plotted in Fig. 11(a). Similar to Fig. 5(a), the dotted line envelope represents the maximum efficiency that can be achieved through adjusting F (hereby referred to as the achievable efficiency). The overall trend of the measured achievable efficiency matches the simulation results presented in section II-A and section III-A very well, with the peak efficiency and 3 dB roll-off occurring at around $z=5$ cm and $z=9$ cm respectively, and the focal distance tuning range being roughly within 14 cm. The measured peak efficiency is around 4% at $z=5$ cm (4.6 times the receiver diameter) with F set as 5 cm, corresponding to an ATF of around 20%. Similar to the simulation results, the increase in efficiency through focusing can clearly be seen when compared to the case with no focusing applied to the array transducers (constant phase to all 37 array elements). For a more valid comparison, the measurement results using the entire 37 element array with F set as 5 cm is also compared to the measurement results when only activating the center 19 array elements with no focusing applied (constant phase to the center 19 elements), as plotted in the Fig. 11(b). The latter case (only activating the center 19 elements with no focusing applied) is used to mimic a single large transducer with diameter around 5 cm, which has a peak efficiency near 6 cm. Compared at peak efficiency, the case with F set as 5 cm applied to the 37 element array provides a 2.6 times increase in efficiency compared to the case with only the center 19 elements activated and no focusing applied. This demonstrates that phased array transmitters can be used to increase the efficiency throughout the near-field region, and by adjusting F, efficiency can be maintained relatively constant up to the 3dB roll-off distance. For our current setup, the input power to each array transducer was within 10 mW (limited by the driving circuit), therefore the maximum output power received was 15 mW; the current setup was designed to showcase improvements in efficiency, rather than output power, but a higher output power would also be possible for a system designed to maximize output power.

The measured overall efficiency was also compared to the numerical simulations, with the simulated overall efficiency estimated by using the measured transducer efficiencies stated in section IV-A. For the case with F set as 5 cm, the comparison between measurements and simulations is shown in Fig. 12(a) (including simulations for both the 37 element array and the simplified $N=4$ ring array). The measurements in this case were taken with finer axial sampling points along the distance z direction to understand possible standing wave effects. As shown, the measured efficiency curve closely matches the trend of the simulation results, but the simulations predicted an efficiency 1.5 times higher than the measured efficiency of 4%.

This discrepancy may be due to the fact that the Butterworth-van Dyke model used for the transducers does not account for frequency dependent wave reflections (as mentioned in section IV-A). Although the reflections measured from our current setup are relatively small, it may have contributed to the discrepancy. Another possible culprit for the discrepancy may be due to the imperfect estimation of the receiver effective transducer area.
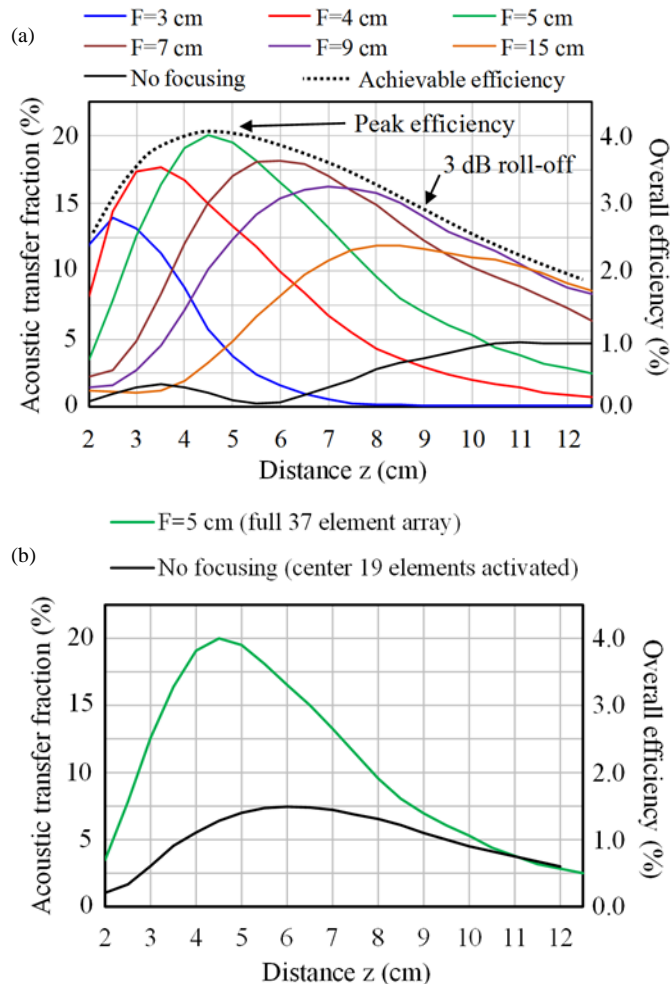

Fig. 11. Measurement results: (a) Overall efficiency and ATF versus distance z with various F values, (b) comparison between using the entire 37 element array with $F=5$ cm and only activating the center 19 elements with no focusing applied (equivalent to a single large transducer with $D\sim5$ cm).

Note that with the refined distance measurement points, small variations within the measured efficiency curve can be observed, as shown in Fig. 12(a). This is due to the acoustic impedance mismatch at the transducers, causing a certain percentage of the acoustic power to be reflected between the transmitter and receiver, leading to spatial resonances (standing waves) in efficiency with regard to the receiver distance, as described in [26], [28]. For the 37 element array, due to the different path lengths from each individual array transducer to the receiver, the spatial resonances do not always occur with a constant $\lambda/2$ distance spacing. Note that the reflections are not severe in our construction, as the spatial resonances only lead to at most a 6% fluctuation in observed efficiency near the peak

efficiency (z=5 cm), while the fluctuations in efficiency at other distances are much less significant. As mentioned in section II, this serves to justify our usage of the current transducer model which does not take into account reflections.
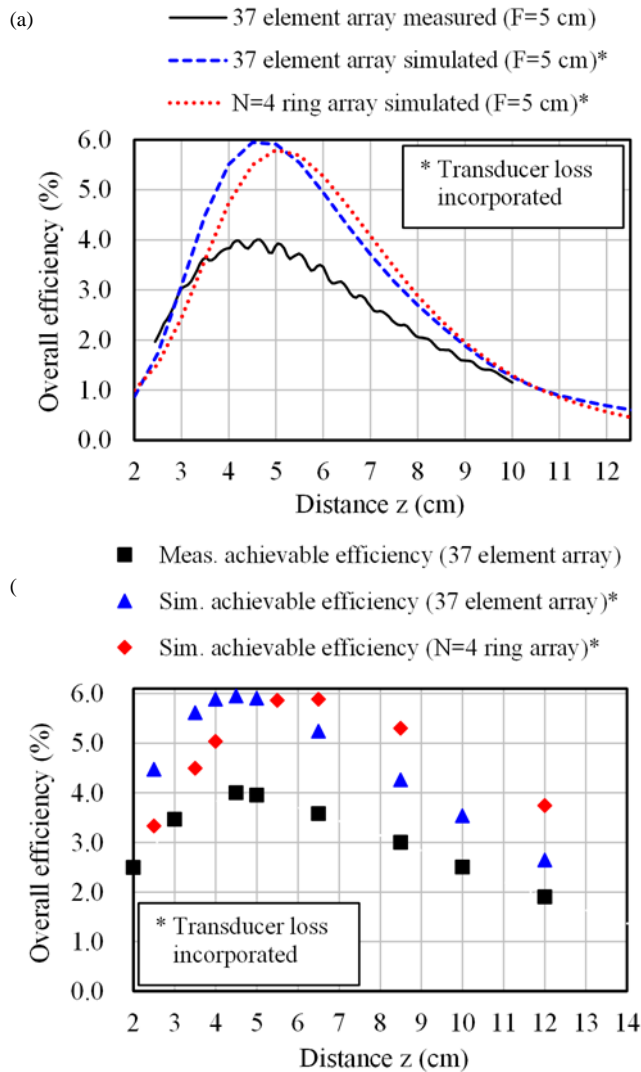

Fig. 12. Measurement results: (a) Comparison between measured efficiency (finer distance z sampling) and simulated efficiencies (all with F=5 cm), (b) comparison between the measured and simulated achievable efficiency (envelope of Fig. 9(a) and Fig. 5(a)).

Finally, for both the measurement results and simulation results, data points occurring on the envelope (i.e. the achievable efficiency) were chosen and plotted together for comparison in Fig. 12(b). As shown, for the 37 element array, the measured achievable efficiency also matches the simulated trend very well, with the peak efficiency and 3dB roll-off occurring at the same distances as the simulation results, while the simulation results for the N=4 ring array has a slightly larger peak efficiency and 3dB roll-off distance.

C. Comparison to Inductive WPT

In order to verify that the phased array acoustic WPT system performs better than an inductive WPT system at larger distances, inductive transmitting and receiving coils were also built and tested. For a fair comparison, the diameter of the transmitting coil was set to be the same as the ultrasonic phased array (7 cm diameter), and the diameter of the receiving coil was set to be the same as the receiver transducer (1.1 cm diameter). This type of inductive WPT from larger coils to smaller coils has been used to power multiple devices on a platform [41], [42]. Due to the smaller diameter of the receiving coil, less magnetic flux is coupled between the transmitter and receiver [41], which limits the inductive WPT efficiency. Enameled copper wire with 270 μm diameter was used to construct the coils, and to investigate the effect of the number of turns, the transmitting and receiving coils were both either 6 turns or 12 turns. The best turn ratio combination to maximize efficiency was found to be the case with 6 turns for the transmitting coil and 12 turns for the receiving coil (similar to the turn ratio in [41]).

For magnetic resonant inductive WPT loading conditions [24], the maximum efficiency η_{opt_IPT} that can be achieved with the optimal load $R_{L\_opt\_IPT}$ can be expressed as [43]

$$\eta_{opt\_IPT} = \frac{k^2 Q_1 Q_2}{\left(1+\sqrt{1+k^2 Q_1 Q_2}\right)^2} \tag{5}$$

$$R_{L\_opt\_IPT} = R_2 \sqrt{1+k^2 Q_1 Q_2} \tag{6}$$

with k as the coupling coefficient between the coils, Q_1/Q_2 as the quality factor of the transmitting/receiving coil, and R_2 as the series resistance for the receiving coil. Note that the matching capacitors are assumed to be ideal in this case, therefore η_{opt_IPT} represents the theoretical maximum inductive WPT efficiency that can be achieved. A Keysight E5061B network analyzer was then used to measure the k, Q_1, and Q_2 between the 6 turn transmitting coil and 12 turn receiving coil at different distances. The frequency at which the maximum inductive WPT efficiency η_{opt_IPT} is achieved was found to be near 7 MHz, at which the quality factors of the coils were Q_1=84 for the transmitter coil and Q_2=67 for the receiver coil, which is reasonably good compared to coils of similar dimensions in other work [6], [9]. The resulting maximum inductive WPT efficiency η_{opt_IPT} was plotted with the measured achievable efficiency for the phased array acoustic WPT system in Fig. 13. As shown, the inductive WPT efficiency drops rapidly as distance increases, and at distances above 5 cm, the acoustic WPT efficiency outperforms the inductive WPT efficiency. At 10 cm, the acoustic WPT efficiency is 18 times the inductive WPT efficiency.

D. Beam Angle Steering

Another benefit of using a phased array transmitter is that beam angle steering could also be used to direct power to receivers located at arbitrary angles off the main axis of the transmitter array. To demonstrate beam angle steering, a simplified 7 element 1D linear array was designed and constructed, with the smaller number of elements allowing simpler phase control; the full 37 element array would have required 20 separate phases to beam steer around one axis. The experimental setup is shown in Fig. 14. A test arc with mounting holes was 3D printed to allow the receiver to be fixed
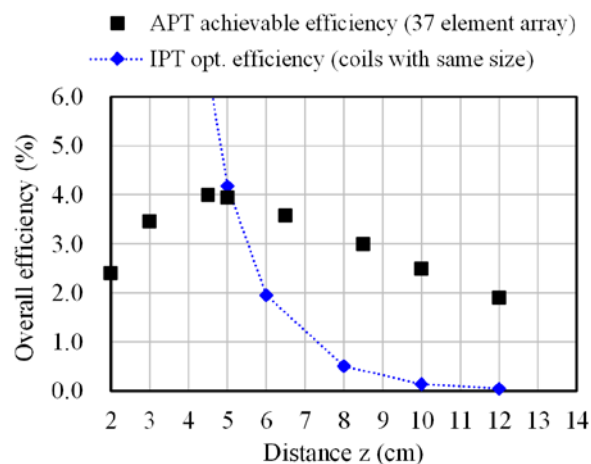
Fig. 13. Measured achievable efficiency for acoustic power transfer (APT) versus optimal efficiency for inductive power transfer (IPT) with equal size.
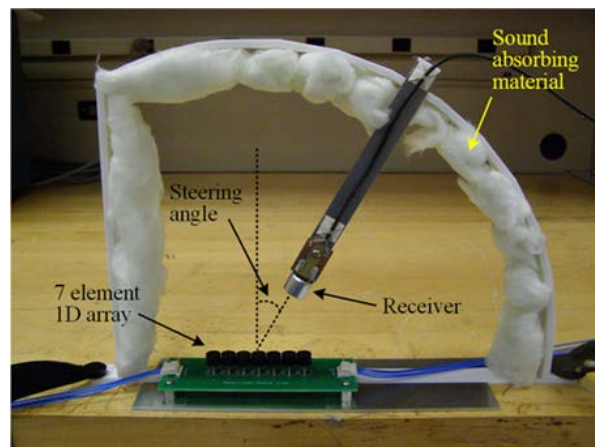

Fig. 14. Experimental setup for the beam angle steering measurements using the 7 element 1D array and the small receiver mounted on a test arc.
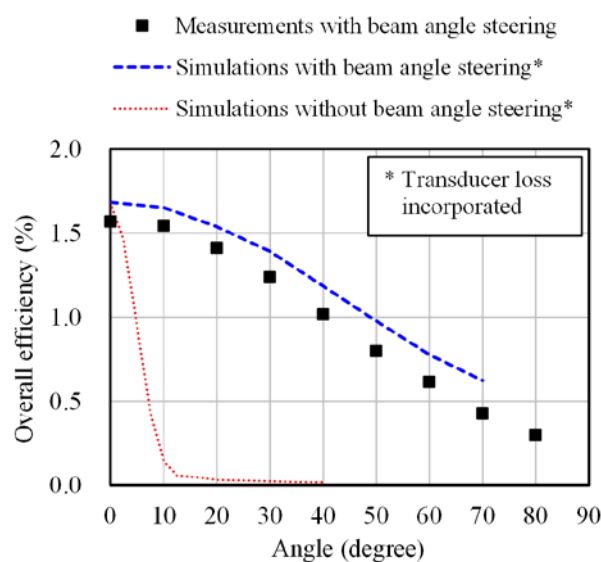

Fig. 15. Comparison between measured efficiency and simulated efficiency versus angle using the 7 element 1D array (z=5 cm).

at different angles while maintaining a constant 5 cm distance from the center of the 7 element 1D array. Sound absorbing material was used to cover the inner surface of the test arc to avoid reflections. The phase delay of each array transducer element was adjusted to have the beam steering angle match the angle at which the receiver is fixed at, with the steering angle defined as shown in Figure 14.

Simulations were also compared to the measurement results, as shown in Fig. 15, with the simulated overall efficiency again calculated by using the measured transducer efficiencies. Due to the lesser number of elements, the measured peak efficiency achieved at 0 degrees is lower at around 1.6%. As shown, the measurement results correspond well with the simulation results, with the measured efficiencies being slightly lower than the simulated efficiencies (the difference being more significant at larger angles). This is possibly due to the narrower than expected radiation angle from each array transducer as well as inaccuracies in the phase adjustments for beam angle steering. As the steering angle increases, the achievable efficiency gradually decreases due to the limited radiation angle from each array transducer. The achievable efficiency through beam angle steering roughly drops to around 50% of the peak efficiency at 50 to 60 degrees. Without beam angle steering (constant phase to all 7 transducer elements), the simulation results are also plotted in Fig. 15, showing that the efficiency quickly drops to below 0.14% (a 90% drop from the peak efficiency) when the receiver is at 10 degrees. From the comparison in Fig. 15, it can be seen that the measured efficiency with beam steering quickly outperforms the simulated efficiency without beam steering when the angle increases. Note that since the 37 element array has more transducers in the outer array portion than the 7 element 1D array, the effect of the narrower transducer radiation angle becomes more significant, serving as one possible explanation as to why the measurements and simulations correspond better in Fig. 15 than in Fig. 12(a).

To further showcase the advantage of phased array beam steering, the measured ATF versus angle from the 7 element 1D array with beam steering was compared to the simulated ATF

versus angle from a single large transducer with 4.5 cm diameter, as plotted in Fig. 16 (both at a constant 5 cm distance). As mentioned in section II-A, the 4.5 cm diameter single large transducer has a peak efficiency distance close to 6 cm, therefore serving as a more valid comparison. At 0 degrees, the 4.5 cm diameter single transducer provides a higher ATF. However, when the angle is above 10 degrees, the 7 element 1D array starts to outperform the 4.5 cm diameter single transducer. At 40 degrees, the measured ATF from the 7 element 1D array is 27 times higher than the simulated ATF from the 4.5 cm diameter single transducer. This shows that even without using the full 37 element array, the 7 element 1D array can achieve a higher ATF than the single large transducer at larger angles, successfully demonstrating that phased array transmitters can provide power transfer less dependent on receiver placement.

V. CONCLUSION

The feasibility of utilizing ultrasonic phased array transmitters to improve the performance of wireless power
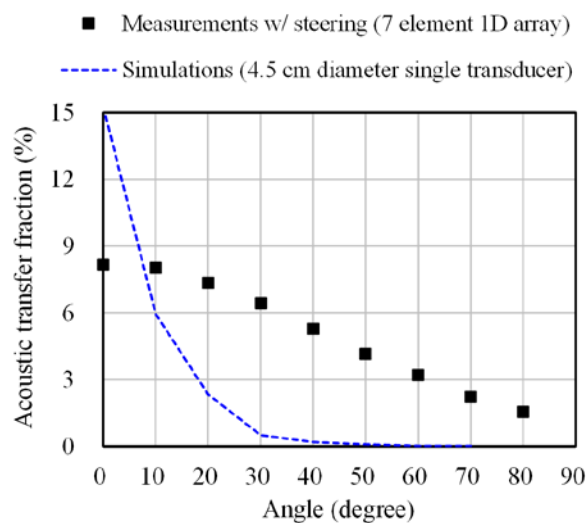
Fig. 16. Measured ATF versus angle for the 7 element 1D array with beam steering compared to simulated ATF versus angle for the 4.5 cm diameter single transducer (at z=5 cm).

transmission through airborne acoustic waves was successfully demonstrated, with measurement results shown to correspond well with modeling results. A 37 element phased array transmitter with 7 cm diameter was used to focus power to a receiver with 1.1 cm diameter, greatly increasing the power transfer efficiency at any point within the near-field region (up to 14 cm). The measured peak overall efficiency was 4% (peak ATF of 20%), occurring at a distance of 5 cm (4.6 times the diameter of the receiver), which is a 2.6 times increase in efficiency when compared to the case with no focusing applied (equivalent to a single large transducer with the same peak efficiency distance). For comparison, an inductive WPT system with coils of equivalent diameters as the ultrasonic phased array transmitter and receiver was built and tested, verifying that acoustic WPT can achieve higher efficiencies than inductive WPT at larger distances. To improve the overall acoustic WPT efficiency, a receiver design with better matching and a microfabricated array with hexagonal shaped transducers to increase the number of elements and maintain high fill factor is desired. Within the current dimensions, modeling results predict that an overall efficiency up to 22% is achievable (55% ATF, 63% transmitter and receiver efficiency). The feasibility of beam angle steering was also demonstrated with a 7 element 1D array, achieving power transfer less influenced by receiver placement. Possible future work could be to investigate the far-field behavior for acoustic energy transfer.

REFERENCES

[1] D. Green, "Wireless power receiver market report – 2016", *IHS Markit*, London, UK, Mar. 2016. Available online: technology.ihs.com

[2] J. Shin, S. Shin, Y. Kim, S. Ahn, S. Lee, G. Jung, S.-J. Jeon, and D.-H. Cho, "Design and Implementation of Shaped Magnetic-Resonance-Based Wireless Power Transfer System for Roadway-Powered Moving Electric Vehicles," *IEEE Trans. Ind. Electron.*, vol. 61, no. 3, pp. 1179–1192, Mar. 2014.

[3] E. Waffenschmidt and T. Staring, "Limitation of inductive power transfer for consumer applications," in *13th European Conference on Power Electronics and Applications, 2009*, Barcelona, Spain, 2009.

[4] P. Li and R. Bashirullah, "A wireless power interface for rechargeable battery operated medical implants," *IEEE Trans. Circuits Syst. II, Exp. Briefs*, vol. 54, no. 10, pp. 912–916, Oct. 2007.

[5] P. Si, A. P. Hu, S. Malpas, and D. Budgett, "A frequency control method for regulating wireless power to implantable devices," *IEEE Trans. Biomed. Circuits Syst.*, vol. 2, no. 1, pp. 22–29, Mar. 2008.

[6] A. K. RamRakhyani, S. Mirabbasi, and M. Chiao, "Design and optimization of resonance-based efficient wireless power delivery systems for biomedical implants," *IEEE Trans. Biomed. Circuits Syst.*, vol. 5, no. 1, pp. 48–63, Feb. 2011.

[7] A. Denisov and E. Yeatman, "Ultrasonic vs. inductive power delivery for miniature biomedical implants," in *2010 International Conference on Body Sensor Networks (BSN)*, Singapore, Jun. 2010, pp. 84–89.

[8] S. Ozeri and D. Shmilovitz, "Simultaneous backward data transmission and power harvesting in an ultrasonic transcutaneous energy transfer link employing acoustically dependent electric impedance modulation," *Ultrasonics*, vol. 54, no. 7, pp. 1929–1937, Sep. 2014.

[9] A. Sanni, A. Vilches, and C. Toumazou, "Inductive and ultrasonic multi-tier interface for low-power, deeply implantable medical devices," *IEEE Trans. Biomed. Circuits Syst.*, vol. 6, no. 4, pp. 297–308, Aug. 2012.

[10] S. Li and C. C. Mi, "Wireless power transfer for electric vehicle applications," *IEEE Journal of Emerging and Selected Topics in Power Electronics*, vol. 3, no. 1, pp. 4–17, Mar. 2015.

[11] M. Budhia, J. T. Boys, G. A. Covic, and C.-Y. Huang, "Development of a single-sided flux magnetic coupler for electric vehicle IPT charging systems," *IEEE Trans. Ind. Electron.*, vol. 60, no. 1, pp. 318–328, Jan. 2013.

[12] J. de Boeij, E. Lomonova, J.L. Duarte, and A.J.A. Vandenput, "Contactless power supply for moving sensors and actuators in high-precision mechatronic systems with long-stroke power transfer capability in x–y plane," *Sens. Actuators. A*, vol. 148, no. 1, pp. 319–328, Nov. 2008.

[13] S. Sasaki, K. Tanaka, and K.-I. Maki, "Microwave power transmission technologies for solar power satellites," *Proceedings of the IEEE*, vol. 101, no. 6, pp. 1438–1447, Jun. 2013.

[14] W. C. Brown, "The history of power transmission by radio waves," *IEEE Trans. Microw. Theory Techn.*, vol. 32, no. 9, pp. 1230–1242, Sep. 1984.

[15] W. C. Brown and E.E. Eves, "Beamed microwave power transmission and its application to space," *IEEE Trans. Microw. Theory Techn.*, vol. 40, no. 6, pp. 1239–1250, Jun. 1992.

[16] K. M. Farinholt, G. Park, and C. R. Farrar, "RF energy transmission for a low-power wireless impedance sensor node," *IEEE Sensors J.*, vol. 9, no. 7, pp. 793–800, Jul. 2009.

[17] N. Shinohara, "Beam control technologies with a high-efficiency phased array for microwave power transmission in Japan," *Proceedings of the IEEE*, vol. 101, no. 6, pp. 1448–1463, Jun. 2013.

[18] T. Blackwell, "Recent demonstrations of Laser power beaming at DFRC and MSFC," *AIP Conference Proceedings*, vol. 766, no. 73, pp. 73–85, 2005.

[19] M. Choi, J.-R. Lee, and C.-Y. Park, "Development of a laser-powered wireless strain gauge device using a continuous-wave laser and photovoltaic cell," *J. Intell. Mater. Syst.*, vol. 27, no. 17, pp. 2333–2343, Oct. 2016.

[20] A. Sahai and D. Graham, "Optical wireless power transmission at long wavelengths," in *2011 International Conference on Space Optical Systems and Applications (ICSOS)*, Santa Monica, CA, USA, May 2011, pp. 164–170.

[21] J. Dai and D. C. Ludois, "A survey of wireless power transfer and a critical comparison of inductive and capacitive coupling for small gap applications," *IEEE Trans. Power Electron.*, vol. 30, no. 11, pp. 6017–6029, Nov. 2015.

[22] Z. N. Low, R. A. Chinga, R. Tseng, and J. Lin, "Design and test of a high-power high-efficiency loosely coupled planar wireless power transfer system," *IEEE Trans. Ind. Electron.*, vol. 56, no. 5, pp. 1801–1812, May 2009.

[23] S. Y. R. Hui, W. Zhong, and C. K. Lee, "A critical review of recent progress in mid-range wireless power transfer," *IEEE Trans. Power Electron.*, vol. 29, no. 9, pp. 4500–4511, Sep. 2014.

This article has been accepted for publication in a future issue of this journal, but has not been fully edited. Content may change prior to final publication. Citation information: DOI 10.1109/TUFFC.2017.2771283, IEEE Transactions on Ultrasonics, Ferroelectrics, and Frequency Control

> REPLACE THIS LINE WITH YOUR PAPER IDENTIFICATION NUMBER (DOUBLE-CLICK HERE TO EDIT) <   11

[24] A. Kurs, A. Karalis, R. Moffatt, J. D. Joannopoulos, P. Fisher, M. Soljacic, "Wireless power transfer via strongly coupled magnetic resonances," *Science*, vol. 317, no. 5834, pp. 83–86, Jul. 2007.

[25] T. Ishiyama, Y. Kanai, J. Ohwaki, and M. Mino, "Impact of a wireless power transmission system using an ultrasonic air transducer for low-power mobile applications," in *2003 IEEE Symposium on Ultrasonics*, Honolulu, HI, USA, Oct. 2003, pp. 1368–1371.

[26] M. G. L. Roes, M. A. M. Hendrix, and J. L. Duarte, "Contactless energy transfer through air by means of ultrasound," in *IECON 2011 - 37th Annual Conference on IEEE Industrial Electronics Society*, Melbourne, Australia, Nov. 2011, pp. 1238–1243.

[27] M. G. L. Roes, J. L. Duarte, M. A. M. Hendrix, and E. A. Lomonova, "Acoustic energy transfer: A review," *IEEE Trans. Ind. Electron.*, vol. 60, no. 1, pp. 242–248, Jan. 2013.

[28] M. G. L. Roes, "Exploring the potential of acoustic energy transfer," Ph.D. dissertation, Dept. Elect. Eng., Eindhoven University of Technology, Eindhoven, Netherlands, 2015.

[29] T. C. Chang, M. J. Weber, M. L. Wang, J. Charthad, B. T. Khuri-Yakub, and A. Arbabian "Design of tunable ultrasonic receivers for efficient powering of implantable medical devices with reconfigurable power loads," *IEEE Trans. Ultrason., Ferroelect., Freq. Control*, vol. 63, no. 10, pp. 1554–1562, Oct. 2016.

[30] X. Bao, W. Biederman, S. Sherrit, M. Badescu, Y. Bar-Cohen, C. Jones, J. Aldrich, and Z. Chang, "High-power piezoelectric acoustic-electric power feedthru for metal walls," in *Proc. SPIE, Industrial and Commercial Applications of Smart Structures Technologies 2008*, San Diego, CA, USA, Mar. 2008, vol. 6930, pp. 69300Z.

[31] T. J. Lawry, G. J. Saulnier, J. D. Ashdown, K. R. Wilt, H. A. Scarton, S. Pascarelle,and J. D. Pinezich, "Penetration-free system for transmission of data and power through solid metal barriers," in *2011 Military Communications Conference (MILCOM 2011)*, Baltimore, MD, USA, Nov. 2011, pp. 389–395.

[32] H. Hu, Y. Hu, C. Chen, and J. Wang, "A system of two piezoelectric transducers and a storage circuit for wireless energy transmission through a thin metal wall," *IEEE Trans. Ultrason., Ferroelect., Freq. Control*, vol. 55, no. 10, pp. 2312–2319, Oct. 2008.

[33] S.-C. Wooh and Y. Shi, "Optimization of ultrasonic phased arrays," in *Review of Progress in Quantitative Nondestructive Evaluation*, vol. 17A, New York, Springer US, 1998, pp. 883–890.

[34] S.-C. Wooh and L. Azar, "Phase steering and focusing behavior of ultrasound in cementitious materials," in *Review of Progress in Quantitative Nondestructive Evaluation*, vol. 18A, New York, Springer US, 1999, pp. 2161–2168.

[35] T. Iwamoto, M. Tatezono, and H. Shinoda, "Non-contact method for producing tactile sensation using airborne ultrasound," in *Proc. EuroHaptics 2008*, Madrid, Spain, Jun. 2008, pp. 504-513.

[36] L.-C. Cheng, Y.-C. Kang, and C.-L. Chen, "A resonance-frequency-tracing method for a current-fed piezoelectric transducer," *IEEE Trans. Ind. Electron.*, vol. 61, no. 11, pp. 6031–6040, Nov. 2014.

[37] H. E. Bass, L. C. Sutherland, A. J. Zuckerwar, D. T. Blackstock, and D. M. Hester, "Atmospheric absorption of sound: Further developments," *J. Acoust. Soc. Am.*, vol. 97, no. 1, pp. 680–683, Jan. 1995.

[38] T. L. Szabo, "Array beamforming," in *Diagnostic Ultrasound Imaging: Inside Out*, Cambridge, Elsevier Academic Press, 2004, pp. 182–185.

[39] MA40S4S ultrasonic transducer datasheet. Murata Manufacturing Co., Kyoto, Japan. [Online]. Available: http://www.murata.com/en-us/api/pdfdownloadapi?cate=&partno=MA40S4S.

[40] I. Ladabaum, X. Jin, H. T. Soh, A. Atalar, and B. T. Khuri-Yakub, "Surface micromachined capacitive ultrasonic transducers," *IEEE Trans. Ultrason., Ferroelect., Freq. Control*, vol. 45, no. 3, pp. 678–690, May 1998.

[41] B. L. Cannon, J. F. Hoburg, D. D. Stancil, and S. C. Goldstein, "Magnetic resonant coupling as a potential means for wireless power transfer to multiple small receivers," *IEEE Trans. Power Electron.*, vol. 24, no. 7, pp. 1819–1825, Jul. 2009.

[42] T. Deyle and M. Reynolds, "Surface based wireless power transmission and bidirectional communication for autonomous robot swarms," in *Proc. IEEE Int. Conf. Robot. Autom. (ICRA, 2008),* Pasadena, CA, USA, May, 2008, pp. 1036–1041.

[43] M. Zargham and P. G. Gulak, "Maximum achievable efficiency in near-field coupled power-transfer systems," *IEEE Trans. Biomed. Circuits Syst.*, vol. 6, no. 3, pp. 228–245, Jun. 2012.